Multispectral High Dynamic Range Imaging

Johannes Brauers and Nils Schulte and André Alexander Bell and Til Aach

Institute of Imaging and Computer Vision
RWTH Aachen University, 52056 Aachen, Germany
tel: +49 241 80 27860, fax: +49 241 80 22200
web: www.lfb.rwth-aachen.de

in: IS&T/SPIE Electronic Imaging. See also BibTeX entry below.

BibTeX:

```
@inproceedings{BRA08a,
  author    = {Johannes Brauers and Nils Schulte and Andr\'{e} Alexander Bell and Til Aach},
  title     = {Multispectral High Dynamic Range Imaging},
  booktitle = {IS\&T/SPIE Electronic Imaging},
  year      = {2008},
  address   = {San Jose, California, USA},
  month     = {Jan},
  pages     = {680704-1--680704-12}
}
```

RWTHAACHEN
RHEINISCH-WESTFÄLISCHE TECHNISCHE HOCHSCHULE AACHEN

Multispectral High Dynamic Range Imaging

Johannes Brauers, Nils Schulte, André A. Bell, Til Aach

Institute of Imaging and Computer Vision, RWTH Aachen University
Templergraben 55, 52056 Aachen, Germany

ABSTRACT

Capturing natural scenes with high dynamic range content using conventional RGB cameras generally results in saturated and underexposed and therefore compromising image areas. Furthermore the image lacks color accuracy due to a systematic color error of the RGB color filters. The problem of the limited dynamic range of the camera has been addressed by high dynamic range imaging[1,2] (HDRI): Several RGB images of different exposures are combined into one image with greater dynamic range. Color accuracy on the other hand can be greatly improved using multispectral cameras,[3] which more accurately sample the electromagnetic spectrum. We present a promising combination of both technologies, a high dynamic range multispectral camera featuring a higher color accuracy, an improved signal to noise ratio and greater dynamic range compared to a similar low dynamic range camera.

1. INTRODUCTION

Color accuracy in terms of exact reproduction of the electromagnetic spectrum is rarely the decisive factor for consumers when purchasing a camera. Common digital RGB cameras provide a satisfying color reproduction and – perhaps more importantly – are cheap and robust due to their mass-production state, therefore being established in mobiles phones up to professional cameras. It is rarely known that they exhibit a systematic color error[4] as they violate the Luther rule,[5] which states that the camera's spectral sensitivities have to be a linear combination of those of the CIE observer. This makes them unsuitable for the accurate measurement of color, e.g. of art paintings.[6]

Another drawback of the most common camera type, namely the 1-chip RGB camera, is its need for spatial interpolation of color information: Since 1-chip color cameras are equipped with a color filter array (CFA) mapping three spectral sensitivities to the spatial domain, this results in a downsampled image for each color channel. Though by using an interpolation algorithm,[7] the separated color channels can be recombined into one color image, interpolation artifacts remain. Another disadvantage of the CFA is the induced shift variance,[8] which causes the image statistics to be dependent on the image shift.

Figure 1. Our multispectral camera (left) and a sketch of its internal configuration (right).

Further author information: (Send correspondence to Johannes Brauers.)
Johannes Brauers: E-mail: Johannes.Brauers@lfb.rwth-aachen.de, Telephone: +49 (241) 80 27866

Our multispectral camera shown in Fig. 1 offers a greatly improved color accuracy compared to 1-chip RGB cameras since the complete spatial information is acquired for each of seven color channels: This is achieved by placing a computer-controlled filter wheel with optical bandpass filters between lens and gray level imaging sensor. For each filter wheel position, gray level images are acquired separately and are combined into a multispectral color image afterwards. This enables a rough sampling of the electromagnetic spectrum, and the Luther rule mentioned above is mostly fulfilled. However, only static scenes can be acquired by this technique.

A problem concerning all conventional cameras – including gray level cameras – is their limited dynamic range. This means that the acquisition of scenes with a high dynamic range (HDR) results in saturated as well as underexposed areas. The latter furthermore contain more noise and a lower signal to noise ratio. Since our multispectral camera internally uses an industrial gray level camera, it is affected by the problem as well. We extend the dynamic range by using high dynamic range imaging:[1, 2] For each filter wheel position, we acquire several images with different exposures by varying the exposure time. The images are then combined into a multispectral high dynamic range (MHDR) image.

An interesting approach[9] of multispectral HDR imaging using two 3CCD RGB cameras is accomplished by use of a half mirror to present the same view to both cameras, which are arranged perpendicularly. The ability to acquire multispectral images is given by using different interference filters which split the original passbands each into two halves. By doing so, e.g., the lower half of the red spectral sensitivity is acquired by the first camera and the higher half by the second camera. High dynamic range imaging is enabled by placing an additional neutral density filter in front of one camera. The outcome of this is that three passband halves are acquired with full sensitivity, while the other ones are acquired with a reduced sensitivity due to the neutral density filter. Therefore, the innovative concept in [9] offers only the limited number of two exposure levels, which may not suffice for many HDR applications. Another limitation occurs when one half of a passband is saturated: In this case, there is no estimation for that specific wavelength range at all, since the passband halves are shared by both cameras. In contrast, our concept is not limited to a certain number of exposure levels, acquires the full spectral range for each exposure level and thus provides a greater dynamic range.

We start by the derivation of a model for the image acquisition chain in section 2 with both a continuous and discrete representation and describe the estimation of spectra. We explain the procedure of image acquisition including calibration, address data export and describe our experiments in section 3 before we present our results in section 4. We conclude with section 5.

2. MODEL

Fig. 2 shows our acquisition model for high dynamic range imaging. The variable symbols are chosen according to [10,11] where applicable. The object $\beta(\lambda)$ * is illuminated by a light source and the reflected light passes through the optics, aperture and is filtered by one of the – in our case – seven spectral bandpass filters which are arranged in a computer-controlled filter wheel. The final camera value $q_{i,j}$ is further influenced by the camera spectral characteristics, sensor size, exposure time and the camera transfer function (CTF), which describes the opto-electronic conversion of the radiant energy to a camera value. By modeling and inverting this optical chain, we derive an estimation of the object reflectance $\beta(\lambda)$ by evaluating the camera output values $q_{i,j}$.

2.1 Mathematical model of the imaging chain

The light source $S(\lambda)$ emits light with the spectral irradiance $S(\lambda)$ (unit: $\frac{W}{m^2 nm}$). It is reflected by the spectral reflectance $\beta(\lambda)$, passes through the optics $o(\lambda)$, which is normally assumed to be $o(\lambda) = 1$ and the aperture, which reduces the spectral irradiance by a constant $a \leq 1^\dagger$. The next optical element is our filter wheel, which contains I optical bandpass filters, where each filter has a specific spectral characteristic curve $\tau_i(\lambda)$, $i = 1 \ldots I$ (see Fig. 3a). Each optical bandpass filter passes only a part of the spectrum and enables us to acquire the spectral color component for that specific wavelength range. The spectral irradiance reaching the sensor surface

---

*In fact, our object is acquired with a spatial resolution $\beta_{x,y}(\lambda)$. Without loss of generality, our model does not incorporate position-dependence and we use the simplified notation $\beta(\lambda)$.

†In fact, the solid angle of the object with respect to the light source and camera has an additional influence on the optical path, but is not considered here. It may be modeled by implicit integration into the aperture constant a.
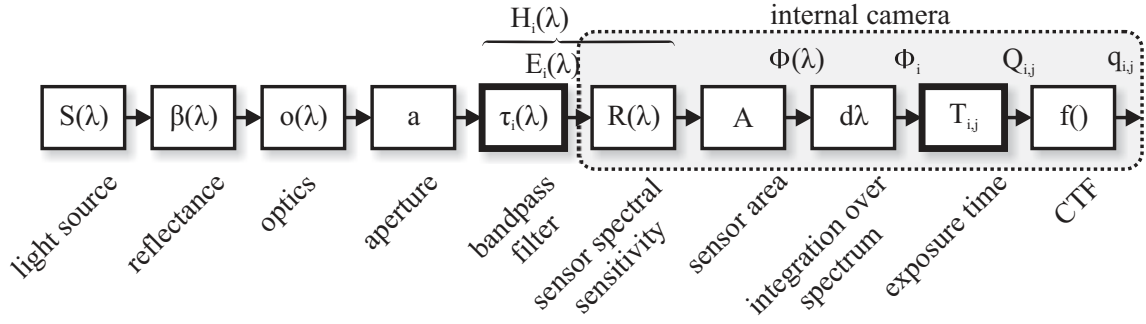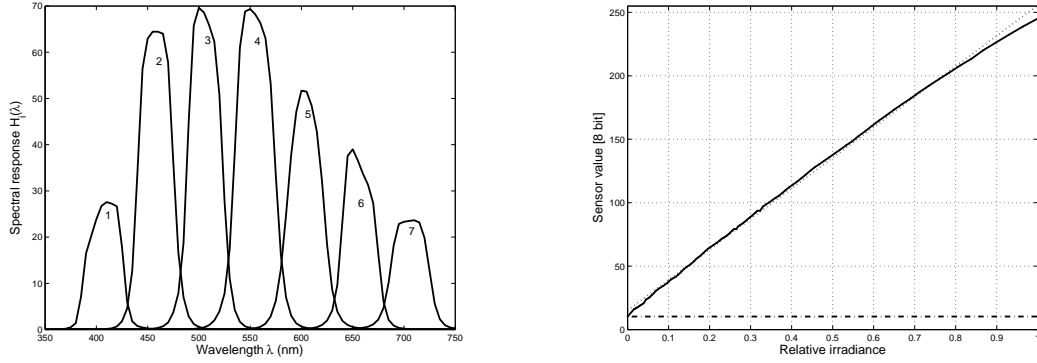
Figure 2. Diagram of our physical model using continuous variables; bandpass filters $\tau_i(\lambda)$ are responsible for spectral resolution, exposure times $T_{i,j}$ for the resolution in the range of values. Abbreviations: $H_i(\lambda) = \tau_i(\lambda)R(\lambda)$, $k = Aa$.

(a) Joint spectral characteristics $H_i(\lambda)$ of optical bandpass filters $\tau_i(\lambda)$ and sensor $R(\lambda)$.

(b) Camera transfer function f of our internal gray level camera Sony XCD-SX900; solid lines denote measurements, the dotted line is a line fit, and the dashed line marks the black level.

Figure 3. Spectral and radiometric characteristic curves of our multispectral camera.

is then derived by

$$E_i(\lambda) = S(\lambda)\,\beta(\lambda)\,o(\lambda)\,a\,\tau_i(\lambda)\ , \tag{1}$$

where the physical unit of $E_i(\lambda)$ is $\frac{\text{W}}{\text{m}^2\text{nm}}$, since the optical elements $\beta(\lambda)$, $o(\lambda)$, a and $\tau_i(\lambda)$ are unit-less. By multiplication of (1) with the spectral characteristic curve $R(\lambda)$ of the sensor and the sensor area A, the spectral radiant power (unit: $\frac{\text{W}}{\text{nm}}$) is computed by

$$\phi(\lambda) = E_i(\lambda)\,R(\lambda)\,A\ . \tag{2}$$

Integrating over the whole wavelength range yields the radiant power

$$\phi_i = \int_\lambda \phi(\lambda)\,d\lambda = \int_\lambda S(\lambda)\,\beta(\lambda)\,o(\lambda)\,a\,\tau_i(\lambda)\,R(\lambda)\,A\,d\lambda \tag{3}$$

for filter i with the physical unit W (Watts). ϕ_i represents a spectral sample, corresponding to a certain wavelength range of our object and we also term it *spectral channel i*. To take different exposure times $T_{i,j}$ with a total number of J exposure levels into account, we compute the radiant energy

$$Q_{i,j} = \phi_i T_{i,j} \tag{4}$$

with the physical unit Ws = J (Joule). We implicitly assume that ϕ_i is not a function of time, i.e., we have a still scene during the acquisition. The final camera value is derived by

$$q_{i,j} = f(Q_{i,j}) \,, \tag{5}$$

where f is the camera transfer function (CTF), which describes the opto-electronic conversion of the radiant energy $Q_{i,j}$ to a camera value $q_{i,j}$. The CTF of our multispectral camera is depicted in Fig. 3b and covers non-linearities of the camera's internal analog/digital converter. It can be precisely measured by the procedure described in section 3.1. Equations (1) to (5) can now be combined into

$$q_{i,j} = f\left(T_{i,j} \int S(\lambda)\,\beta(\lambda)\,o(\lambda)\,a\,\tau_i(\lambda)\,R(\lambda)\,A\,d\lambda \right) \,. \tag{6}$$

To simplify (6), we set $o(\lambda) = 1$, combine the sensor spectral sensitivity $R(\lambda)$ and the filter spectral characteristic $\tau_i(\lambda)$ into $H_i(\lambda) = \tau_i(\lambda)R(\lambda)$, set $k = aA$ and obtain

$$q_{i,j} = f\left(T_{i,j} \int k\,H_i(\lambda)\,S(\lambda)\,\beta(\lambda)d\lambda \right) \,, \tag{7}$$

which describes the complete acquisition procedure in the noiseless case. It depends on the selected bandpass filter i and the exposure channel j.

2.2 Discrete representation of the imaging chain

Because typical reflectance spectra are smooth, it is sufficient and common[3,9,12] to use sampled spectra, e.g., with a number of $N = 61$ spectral samples, which cover a wavelength range from $\lambda_1 = 400$nm to $\lambda_N = 700$nm. Towards this end, we write Eq. (4)-(5) in matrix notation

$$\mathbf{q}_j = f\left(\mathbf{T}_j \boldsymbol{\phi} \right) \,. \tag{8}$$

Inserting

$$\boldsymbol{\phi} = k\mathbf{H}\mathbf{S}\boldsymbol{\beta} \,, \tag{9}$$

yields the complete model

$$\mathbf{q}_j = f\left(\mathbf{T}_j k\mathbf{H}\mathbf{S}\boldsymbol{\beta} \right) \tag{10}$$

from Eq. (7). Note that the integration in (7) is now implicitly realized by a matrix multiplication according to

$$q_{i,j} = f\left(T_{i,j} \sum_{n=1}^{N} k\,H_i(\lambda_n)\,S(\lambda_n)\,\beta(\lambda_n) \right) \,. \tag{11}$$

The bold symbols denote vectors or matrices defined by

$$\mathbf{q}_j = (q_{1,j} \ldots q_{I,j})^T \qquad\qquad (I \times 1)$$
$$\boldsymbol{\phi} = (\phi_1 \ldots \phi_I)^T \qquad\qquad (I \times 1)$$
$$\mathbf{T}_j = \mathrm{diag}\,(T_{1,j} \ldots T_{I,j}) \qquad\qquad (I \times I)$$
$$\mathbf{H}_i = (H_i(\lambda_1) \ldots H_i(\lambda_N))^T \qquad\qquad (N \times 1)$$
$$\mathbf{H} = (\mathbf{H}_1 \ldots \mathbf{H}_I)^T \qquad\qquad (I \times N)$$
$$\mathbf{S} = \mathrm{diag}\,(S(\lambda_1) \ldots S(\lambda_N)) \qquad\qquad (N \times N)$$
$$\boldsymbol{\beta} = (\beta(\lambda_1) \ldots \beta(\lambda_N))^T \qquad\qquad (N \times 1) \,,$$

and correspond to their continuous variables. The operator diag($\cdot$) derives a diagonal matrix from a vector, $()^T$ denotes a transpose operation and I is the number of bandpass filters of the multispectral camera.

2.3 Estimation

Given several camera responses $q_{i,j}$ for different spectral channels $i = 1 \ldots I$ and exposure channels $j = 1 \ldots J$, our aim is to estimate the originating spectrum $\beta(\lambda)$ and its discrete variable $\boldsymbol{\beta}$ respectively, i.e. the inversion of Eq. (10). We split the solution into the HDRI part – namely the inversion of (8) – and the spectral estimation, which corresponds to an inversion of (9).

In the ideal case, without quantization and camera noise and without saturation effects of our camera, we could directly invert Eq. (8), yielding the correct values $\boldsymbol{\phi}$. But in reality, we have to use a weighted averaging

$$
\hat{\phi}_i = \frac{\sum\limits_{j=1}^{J} \frac{f^{-1}(q_{i,j})}{T_{i,j}} w(q_{i,j})}{\sum\limits_{j=1}^{J} w(q_{i,j})} = \frac{\sum\limits_{j=1}^{J} \frac{Q_{i,j}}{T_{i,j}} w(q_{i,j})}{\sum\limits_{j=1}^{J} w(q_{i,j})} \ , \tag{12}
$$

of sensor values $\mathbf{q}_j$. The inverse camera transfer function (ICTF) is denoted by f^{-1} and the weighting function by $w(\cdot)$. The ICTF is the inversion of the CTF depicted in Fig. 3b and compensates camera-specific nonlinearities as well as the black level of the camera. The weighting function $w(\cdot)$ favors values in the center of the range of values over the ones at the borders, suppressing saturated values. Several weighting functions are suggested in the literature; we actually use a Tukey window (see Fig. 4)

$$
w(d) = \begin{cases} 1.0 & 0 \leq |d| \leq \alpha \frac{D}{2} \\ \frac{1}{2}\left(1 + \cos\left(\pi \frac{d - \alpha \frac{D}{2}}{2(1-\alpha)\frac{D}{2}}\right)\right) & \alpha \frac{D}{2} \leq |d| \leq \frac{D}{2} \end{cases} \tag{13}
$$

with a length $D + 1 = 256$ and a taper ratio of $\alpha = 0.5$, because it suppresses the unconfident values in the upper and lower range of values: in the measured CTF in Fig. 3b, especially the border areas diverge from the best fit straight line and the upper area exhibits a rougher quantization, since lesser sensor values are assigned to a fixed irradiance interval. An alternative weighting function is the derivative of the CTF $f'()$,[1,13] which is similar to our weighting function. However, since our CTF is rather linear, the critical border areas would have a too strong influence and so we use the more stringent weighting function in (13) instead.

In practice, Eq. (12) corresponds to a combination of camera images with different exposures but the same spectral channel to single grayscale HDR images. These images exhibit a greater dynamic range than the single images and each one represents a different wavelength range because it was acquired through a specific optical bandpass filter i.
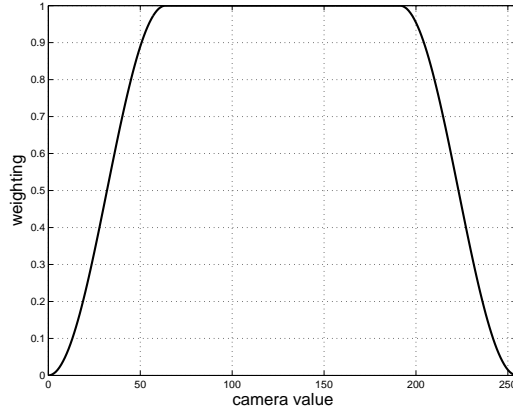

Figure 4. Windowing function $w(\cdot)$: Tukey window with length $D + 1 = 256$ and taper ratio $\alpha = 0.5$.

In most cases, the spectral resolution N (e.g. $N = 61$) is higher than the number of acquired spectral channels I (e.g. $I = 7$). Therefore, Eq. (9) can not be directly inverted as well, yet the reflectance vector $\boldsymbol{\beta}$ has

to be interpolated from the the radiant power $\hat{\phi}$. In other words, equation (9) cannot be inverted because the matrix $\mathbf{H}$ maps an $(N \times 1)$ vector to an $(I \times 1)$ vector. In addition, the light source $\mathbf{S}$ is normally unknown and is estimated from a reference target in our case. We furthermore approximate (9) by introduction of a $(I \times I)$ diagonal light source matrix $\mathbf{S}'$ and derive

$$\phi = k\mathbf{S}'\mathbf{H}\boldsymbol{\beta}\,. \tag{14}$$

Since the real spectral resolution is limited to only I spectral channels, the approximation does not introduce any limitations concerning accuracy, but allows for further simplification in (17).

To determine the spectrum of the light source $S(\lambda)$ and its discrete approximated variable $\mathbf{S}'$ respectively, we acquire a white balance reference card with a known spectrum $\boldsymbol{\beta}_{\mathrm{ref}}$. With knowledge of the camera response $\boldsymbol{\phi}_{\mathrm{ref}}$, we compute

$$\mathbf{S}'_{\mathrm{ref}} = \mathrm{diag}\left(\boldsymbol{\phi}_{\mathrm{ref}} \div (k\mathbf{H}\boldsymbol{\beta}_{\mathrm{ref}})\right)\,, \tag{15}$$

where the operation "$\div$" denotes an element-wise division.

By insertion of (15) into (14), we derive

$$\phi = k\,\mathrm{diag}\left(\boldsymbol{\phi}_{\mathrm{ref}} \div (k\mathbf{H}\boldsymbol{\beta}_{\mathrm{ref}})\right)\mathbf{H}\boldsymbol{\beta} \tag{16}$$

and by further simplification

$$(\phi \div \boldsymbol{\phi}_{\mathrm{ref}}) \circ (\mathbf{H}\boldsymbol{\beta}_{\mathrm{ref}}) = \mathbf{H}\boldsymbol{\beta}\,, \tag{17}$$

where the symbol "$\circ$" denotes an element-wise multiplication. The division of ϕ by $\boldsymbol{\phi}_{\mathrm{ref}}$ can be interpreted as a multispectral white balance and cancels out the camera specific factor k. The validity of (17) can be checked by inserting the white reference card $\boldsymbol{\beta} = \boldsymbol{\beta}_{\mathrm{ref}}$: ϕ then becomes $\boldsymbol{\phi}_{\mathrm{ref}}$ and the equality holds.

Since $\mathbf{H}$ is non-invertible because of its rectangular shape, we have to use an approximation

$$\hat{\boldsymbol{\beta}} = \mathbf{H}_{\mathrm{inv}}\left((\phi \div \boldsymbol{\phi}_{\mathrm{ref}}) \circ (\mathbf{H}\boldsymbol{\beta}_{\mathrm{ref}})\right) \tag{18}$$

by using the weighted pseudoinverse

$$\mathbf{H}_{\mathrm{inv}} = \mathbf{R}_{xx}^{-1}\mathbf{H}^{T}\left(\mathbf{H}\mathbf{R}_{xx}^{-1}\mathbf{H}^{T}\right)\,. \tag{19}$$

The matrix

$$\mathbf{R}_{xx}^{-1} = \begin{pmatrix} 1 & \rho & \rho^2 & \cdots & \rho^{N-1} \\ \rho & 1 & \rho & \cdots & \rho^{N-2} \\ \rho^2 & \rho & 1 & & \vdots \\ & \vdots & & \ddots & \rho \\ \rho^{N-1} & \rho^{N-2} & \cdots & \rho & 1 \end{pmatrix} \tag{20}$$

models the reflectance $\beta(\lambda)$ as being smooth,[3] i.e., neighboring values are assumed to be correlated by a factor ρ. By using the pseudoinverse without weighting, a strong oscillation of the solution might result. A typical value for ρ is 0.98.

3. PRACTICAL CONSIDERATIONS

We used our multispectral camera shown in Fig. 1 for our experiments. The camera features $I = 7$ optical bandpass filters in the range from 400nm to 700nm in steps of 50nm, which can be controlled via the IEEE-1394 bus by the PC. The camera uses the internal grayscale camera Sony XCD-SX900 with a chip size of 6.4mm $\times$ 4.8mm and a resolution of 1280 $\times$ 760 pixel. We use a Nikkor AF-S DX 18-70mm lens on the external F-mount, while the internal camera features a C-mount.

This section discusses four issues: The relative radiometric calibration of our camera, the practical acquisition procedure, the multispectral data export and the tests we performed to measure the improvement of our MHDR technique compared to conventional LDR multispectral imaging.

3.1 Measuring the camera transfer function (CTF)

The combination of camera values $q_{i,j}$ from J different exposures to a single estimated radiant power $\hat{\phi}_i$ as described by Eq. (12) represents a key issue of multispectral high dynamic range imaging. An important condition is the linearization of the camera values, since the direct combination of (non-linear) camera values would introduce severe errors on the final measurement. The linearization requires the precise measurement of the CTF in Eq. (5) and the application of the inverse CTF

$$Q_{i,j} = f^{-1}(q_{i,j}). \tag{21}$$

To obtain the CTF or its inverse several *estimation* methods have been proposed. These estimates rely on a series of different exposures from the same scene. By assuming to know the exposure ratios and introducing a model for the CTF, e.g. a gamma curve, the parameters of the CTF model can be estimated from the joint histograms of exposure pairs.[14] Alternatively, a smoothness constraint has been incorporated instead of a model to estimate the CTF.[2] Other models investigated in the literature include a polynomial approximation,[15] parametric functions,[1, 16, 17] or a constrained piecewise linear model.[18, 19] However, in our case, we use a more precise method, namely a relative radiometric *measurement* with our calibration stand shown in Fig. 5, which allows a more exact measurement[20] of the CTF than, e.g., chart-based measurement methods.[21] We exploit the relation

$$E \sim \frac{r^2}{r^2 + x^2} L \tag{22}$$

between the radiance L $[W/(m^2 sr)]$ of the integrating sphere with opening diameter r and the distance x between light source and camera sensor to vary the irradiance E $[W/m^2]$ impinging on the sensor of the camera, which influences the sensor value $q_{i,j}$ as well. In practice, we position the camera at various distances x, which implicitly correspond to a specific irradiances E and we capture the sensor values $q_{i,j}$. The result of such a measurement is shown in Fig. 3b: the abscissa denotes the irradiance and the ordinate the sensor value. Since the distances x are measured with $50\mu m$ precision by our distance sensor, the measurement is very accurate.
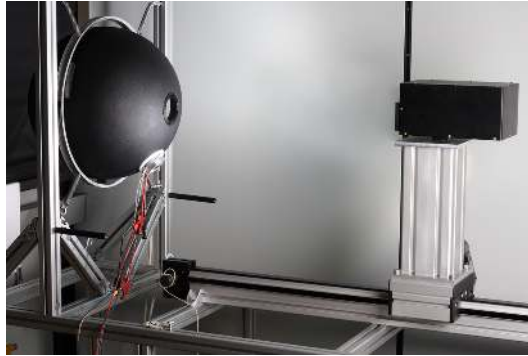

Figure 5. Our camera transfer function (CTF) measurement stand: The integrating sphere (left) illuminates the camera (right); the distance can be modified by shifting the camera and on a sliding carriage (bottom), while the exact position is measured by a distance sensor (not shown).

3.2 Acquisition procedure

Fig. 6 shows all images being acquired when using $J = 3$ different exposure times. The object being captured is a GretagMacbeth ColorChecker with 24 color patches and has been illuminated non-uniformly to produce a high dynamic range scene. In the figure, different exposures have been placed on the vertical axis, while different spectral channels are arranged on the horizontal axis. The reconstruction of the multispectral HDR image is done as follows: First, the geometric distortions between the spectral channels are corrected by an algorithm described in [22]. Towards this end, one channel is defined as the reference channel and a model fit is performed to geometrically adapt the other channels to the reference channel.
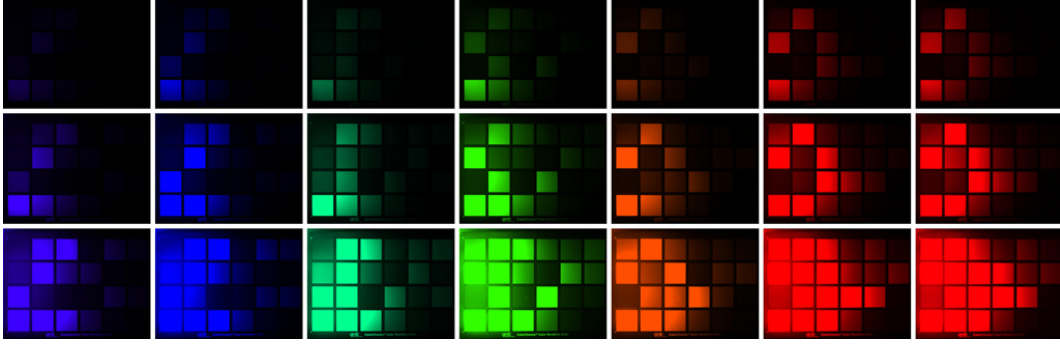
Figure 6. All images taken for an acquisition with seven spectral channels $I = 7$ (left to right) and three exposure levels $J = 3$ (top to bottom).

After that, the inversion of the camera transfer function $f(\cdot)$ and combination to a high dynamic range grayscale image is performed by applying Eq. (12). It can be interpreted as a merging of the images in Fig. 6 on the vertical axis. Fig. 7 visualizes the influence of each image on the HDR image for a series of $J = 7$ exposures: Each histogram represents a single image from the exposure time series, where image values have been normalized with their corresponding exposure time. Images with small exposure times (top of figure) contribute to the reproduction of bright areas of the image, since they occupy a large range of values – yet with a limiting quantization. The rough quantization or rather the sensor's limited resolution causes noise in the dark areas. Images which have been acquired with longer exposure times (bottom of figure) are saturated in the bright areas as the peak on the right indicates. But since they focus their dynamic range on the dark areas, the fine resolution in that areas contributes to the reproduction of dark areas.

To adapt the acquisition to the current light source, a calibration capture of a white reference patch has to be made shortly before the acquisition. The linearized camera response ϕ_{ref} is extracted by cropping and averaging the white balance patch. The calibration counterpart, namely the spectrum β_{ref} can be measured with a spectral photometer.

The final estimation of spectra then is carried out by Eq. (18). The previously estimated white reference data serves as calibration data for the estimation: The term $(\phi \div \phi_{\mathrm{ref}})$ of Eq. (18) represents a multispectral white balance and $((\phi \div \phi_{\mathrm{ref}}) \circ (\mathbf{H}\beta_{\mathrm{ref}}))$ adapts the acquired values to the spectrum β_{ref} of the white reference patch. Finally, the matrix $\mathbf{H}_{\mathrm{inv}}$ interpolates the I-channel camera data to N spectral sample points.

3.3 Multispectral data exchange

We use the `.aix` file format[23] for storing multispectral HDR images, since it provides structures for multichannel images and also copes with floating point data. The floating point data is produced when combining gray scale images to one HDR image as shown in Eq. (12). Reducing the data to, e.g., 8 bit data would destroy the details in dark and bright regions. An advantage of the `.aix` file format is the ability to store the reconstruction matrix $\mathbf{H}_{\mathrm{inv}}$ (see Eq. (19)) within the file. It is therefore not necessary to save the complete reconstructed spectra $\hat{\beta}$ with each e.g. $N = 61$ values but only $I = 7$ channels, resulting in considerable reduction of file size. More precisely, we store the values

$$(\phi \div \phi_{\mathrm{ref}}) \circ (\mathbf{H}\beta_{\mathrm{ref}}) \tag{23}$$

from Eq. (18) in the `Frame` table[23] and the reconstruction matrix $\mathbf{H}_{\mathrm{inv}}$ in the `Samples2Spectrum` table. The spectrum $\hat{\beta}$ is then reconstructed by using the stored matrix $\mathbf{H}_{\mathrm{inv}}$.

3.4 Experiments

For evaluation of the spectral and signal to noise ratio (SNR) performance we utilized a GretagMacbeth *Munsell Digital ColorChecker SG* (see Fig. 8a) featuring 140 color patches with an overall size of 21.6cm × 27.9cm. An intentionally generated shading introduced by halogen lamps causes the scene to exhibit a high dynamic range.
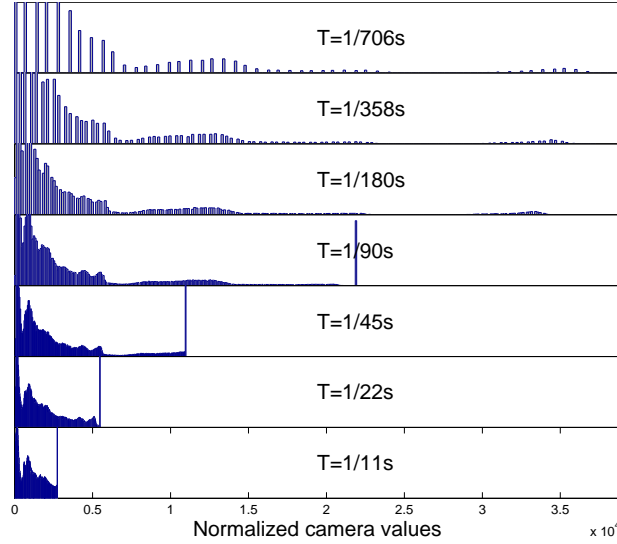
Figure 7. Histograms of normalized images with different exposure times.

We placed the camera perpendicularly to the ColorChecker and acquired $J = 7$ different exposures for the $I = 7$ spectral channels, resulting in a total number of 49 acquisitions.

Because the chosen target also features white patches, we used the patch E5 for white balancing as described in Eq. (15). The reconstruction is then carried out by the equations in section 2. For exact evaluation of each color patch we crop an area inside each patch. To compare our HDR acquisition to an LDR one, we acquire two multispectral images: The first one is an HDR image, where we acquire several exposure levels $j = 1 \ldots 7$. The second one is acquired by using only one exposure level $J = 1$.

4. RESULTS

Fig. 8 visualizes our analysis of the SNR improvement between LDR and HDR acquisition: We measured the peak signal to noise ratio for each patch in both images and computed the differences between LDR patch and HDR patch. We skipped saturated patches in the LDR image since they would seem to have no noise due to the saturation, i.e., the mapping to a single value.

Fig. 8a shows the difference between HDR and LDR patches in terms of SNR; positive numbers denote improvements, negative numbers degradation. The latter ones are due to the introduction of new gray levels in the HDR image: While the resolution in the LDR image is limited and several gray levels are combined into a single level due to quantization, the HDR image provides a greater variety of gray levels. When computing the PSNR, there seems to be more noise in that regions. In general, we derive from Fig. 8a that especially dark patches benefit from HDR imaging. Fig. 8b gives a more statistical view of the SNR improvement and demonstrates the reduction of noise for nearly all color patches. We computed the mean improvement to be 5.06dB for our test image.

Based on the acquired LDR and HDR images, we also investigated on measurements of the color accuracy. The reference spectral data for comparison with the acquired images was collected by scanning the color patches with a GretagMacbeth EyeOne spectral photometer. We measured the color difference between acquisition and reference with the ΔE_{00}[24] formula. To compensate for the shading of our acquisitions and because we are mainly interested in the color components, we scaled the intensity of each image patch to match the original brightness. The results are depicted in Fig. 9, where each point $(\Delta E_{00,\mathrm{LDR}}, \Delta E_{00,\mathrm{HDR}})$ corresponds to one color patch. Points with $\Delta E_{00,\mathrm{LDR}} > \Delta E_{00,\mathrm{HDR}}$ are marked with blue color and represent an improvement in terms of color accuracy, the others denote a degradation. The chart therefore enables a direct impression on the color accuracy improvement of HDR imaging since most of the points are below the diagonal line. More precisely, the color accuracy of 104/140 color patches are improved.

(a) Chart overview. In general, dark patches benefit more from HDR than light patches; saturated fields in the LDR image are left blank.
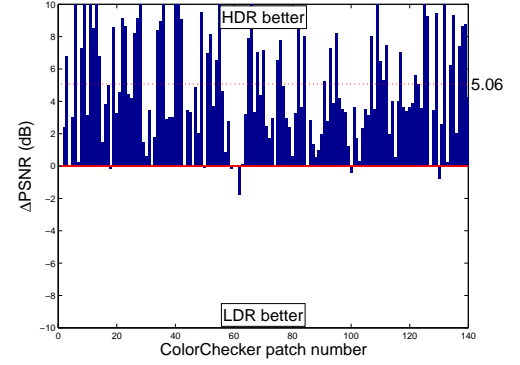
(b) Bar plot. Dotted line denotes mean improvement; saturated fields in the LDR image have been skipped.

Figure 8. Comparison of the signal to noise ratio of LDR/HDR acquisitions of a ColorChecker with 140 color patches, which has been illuminated non-uniformly to simulate a high dynamic range scene. Negative ΔPSNR values are due to introduction of new gray levels in the HDR image.
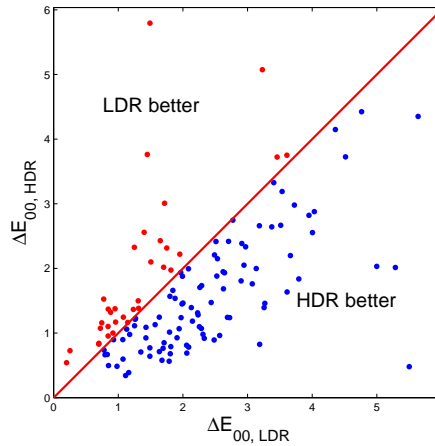

Figure 9. Comparison of spectral error ΔE_{00}: in 104/140 cases, the color accuracy is improved; reference: GTMB EyeOne spectral measure; some data points of $\Delta E_{00,\text{LDR}}$ have been skipped because they are saturated.

To prove practical applicability, we also acquired outdoor scenes with our portable multispectral camera (Fig. 10). Here, also seven exposures have been taken out for each of the seven spectral channels, resulting in a total number of 49 acquisitions. The high image quality can be realized when examining detail crops of dark or bright image regions. Fig. 11a shows a crop of one dormer of Aachen's city hall roof. We artificially brightened the crops to improve the expressiveness. The LDR acquisition exhibits a large amount of noise because the dark regions are mapped only on a few values in the image. Using HDR imaging, the dark regions are also captured with long exposure times, thus mapping the same range of values to more quantization levels (see Fig. 7). The precise information from that exposures for the dark regions is incorporated into the final multispectral HDR image and thus greatly improves image quality.
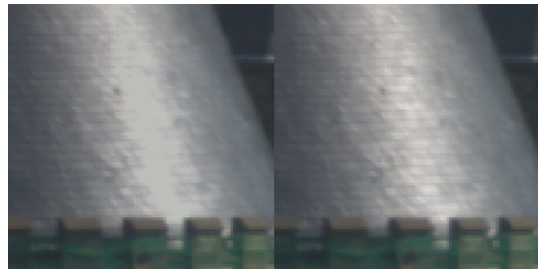
The improvement of light areas as depicted in Fig. 11b is clearer: While bright areas in the LDR image might be saturated due to the limitation of dynamic range, the HDR image also acquires images with short exposure

Figure 10. HDR image of Aachen's city hall.
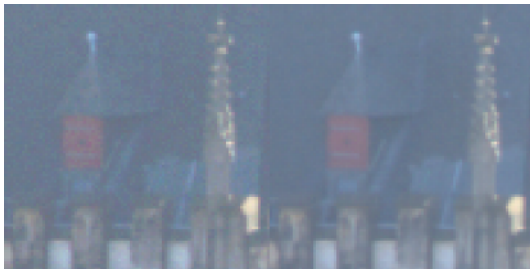
(a) Brightened crops of a dark region: The image noise is significantly reduced.

(b) Shaded crops of a bright region: The HDR image shows more details which are lost in the saturated area of the LDR image.

Figure 11. Detail crops of Fig. 10 showing the improvements of HDR imaging; left images: LDR, right images: HDR.

times coping with bright areas. In the figure, the HDR image therefore preserves the structure of the roof tiles, while it is lost in the LDR image.

5. CONCLUSIONS

We have presented both theory and practice of multispectral high dynamic range (MHDR) imaging: We derived the mathematical model of an MHDR camera and described the spectral estimation from a series of exposures. We presented our camera and addressed several practical issues like the relative radiometric calibration and the spectral calibration with a white patch. In a laboratory test, we compared our camera to a conventional low dynamic range camera and proved the advantages in terms of color accuracy and signal to noise ratio. Additionally, we showed the applicability of our camera by taking outdoor images and emphasized the advantages with descriptive images.

REFERENCES

1. S. Mann, "Comparametric equations with practical applications in quantigraphic image processing," *IEEE Transactions on Image Processing* **9**(8), pp. 1389–1406, 2000.
2. P. E. Debevec and J. Malik, "Recovering High Dynamic Range Radiance Maps from Photographs," in *SIGGRAPH 2007*, pp. 369–378, (Los Angeles, California, USA), Aug 1997.
3. S. Helling, E. Seidel, and W. Biehlig, "Algorithms for spectral color stimulus reconstruction with a seven-channel multispectral camera," in *IS&Ts Proc. 2nd European Conference on Color in Graphics, Imaging and Vision CGIV 2004*, pp. 254–258, (Aachen, Germany), Apr 2004.

4. F. König and P. G. Herzog, "On the limitation of metameric imaging," *Proc. IS&T´s Image Processing, Image Quality, Image Capture, Systems Conference (PICS)* **2**, pp. 163–168, 1999.

5. R. Luther, "Aus dem Gebiet der Farbreizmetrik," *Zeitschrift für technische Physik* **8**, pp. 540–558, 1927.

6. A. Ribés, F. Schmitt, R. Pillay, and C. Lahanier, "Calibration and spectral reconstruction for crisatel: An art painting multispectral acquisition system," *Journal of Imaging Science and Technology* **49**, pp. 563–573, Dec 2005.

7. B. Gunturk, J. Glotzbach, Y. Altunbasak, R. Schafer, and R. Mersereau, "Demosaicking: color filter array interpolation," *IEEE Signal Processing Magazine* **22**, pp. 44–54, January 2005.

8. T. Aach, "Comparative analysis of shift variance and cyclostationarity in multirate filterbanks," *IEEE Transactions on Circuits and Systems–I: Regular Papers* **54**(5), pp. 1077–1087, 2007.

9. H. Haneishi, S. Miyahara, and A. Yoshida, "Image acquisition technique for high dynamic range scenes using a multiband camera," *Wiley's Color Research & Application* **31**(4), pp. 294–302, 2006.

10. G. Wyszecki and W.S.Stiles, *Color Science: Concepts and Methods, Quantitative Data and Formulae*, Wiley, 1982.

11. D. C. O'Shea, *Elements of Modern Optical Design*, Wiley-Interscience, 1985.

12. R. Berns, L. Taplin, M. Nezamabadi, M. Mohammadi, and Y. Zhao, "Spectral imaging using a commercial color-filter array digital camera," in *Proc. of The 14th Triennal ICOM-CC meeting*, pp. 743–750, (The Hague, The Netherlands), Sep 2005.

13. A. A. Bell, J. N. Kaftan, T. Aach, D. Meyer-Ebrecht, and A. Böcking, "High Dynamic Range Images As a Basis for Detection of Argyrophilic Nucleolar Organizer Regions Under Varying Stain Intensities," in *IEEE International Conference on Image Processing, ICIP 2006*, pp. 2541–2544, IEEE, 2006.

14. S. Mann and R. W. Picard, "Being 'undigital' with digital cameras: Extending Dynamic Range by Combining Differently Exposed Pictures," Tech. Rep. 323, M.I.T. Media Lab Perceptual Computing Section, Boston, Massachusetts, 1994.

15. T. Mitsunaga and S. K. Nayar, "Radiometric self calibration," in *IEEE Conference on Computer Vision and Pattern Recognition. CVPR 1999*, **1**, pp. 374–380, 1999.

16. Y. Tsin, V. Ramesh, and T. Kanade, "Statistical calibration of ccd imaging process," in *IEEE International Conference on Computer Vision. ICCV 2001*, **1**, pp. 480–487, 2001.

17. D. Hasler and S. Süsstrunk, "Modeling the Opto-Electronic Conversion Function (OECF) for Application in the Stitching of Panoramic Images," in *International Conference on Imaging Systems (ICIS)*, pp. 379–380, 2002.

18. A. F. Barros and F. M. Candocia, "Image registration in range using a constrained piecewise linear model," in *IEEE International Conference on Acoustics, Speech and Signal Processing. ICASSP 2002*, **4**, pp. 3345–3348, 2002.

19. F. M. Candocia and D. A. Mandarino, "A semiparametric model for accurate camera response function modeling and exposure estimation from comparametric data," *IEEE Transactions on Image Processing* **14**(8), pp. 1138–1150, 2005.

20. A. A. Bell, J. N. Kaftan, D. Meyer-Ebrecht, and T. Aach, "An evaluation framework for the accuracy of camera transfer functions estimated from differently exposed images," in *IEEE Southwest Symposium on Image Analysis and Interpretation*, pp. 168–172, (Denver, Colorado), Mar 2006.

21. Y. C. Chang and J. F. Reid, "Rgb calibration for color image analysis in machine vision," *IEEE Transactions on Image Processing* **5**(10), pp. 1414–1422, 1996.

22. J. Brauers, N. Schulte, and T. Aach, "Modeling and compensation of geometric distortions of multispectral cameras with optical bandpass filter wheels," in *15th European Signal Processing Conference*, (Poznań, Poland), Sep 2007.

23. "Multispectral image file format aix." http://spectral.joensuu.fi/multispectral/spectralimages/AIX-Format-1.6.0.pdf.

24. G. Sharma, W. Wu, and E. N. Dalal, "The CIEDE2000 color-difference formula: Implementation notes, supplementary test data, and mathematical observations," *Wiley's Color Research & Application* **30**, pp. 21–30, Feb 2005.